DIRECT NUMERICAL SIMULATION OF SUPERSONIC TURBULENT FLOW IN AN EXPANSION-COMPRESSION CORNER AT MACH=2.9

Jian Fang[1], Yufeng Yao[2], Lipeng Lu[1], Alexander A. Zheltovodov[3]

[1] National Key Laboratory of Science and Technology on Aero-Engine Aero-Thermodynamics, School of Energy and Power Engineering, Beihang University, Beijing, 100191, China
[2] Faculty of Environment and Technology, Department of Engineering Design and Mathematics, University of the West of England, Bristol, BS16 1QY, United Kingdom
[3] Khristianovich Institute of Theoretical and Applied Mechanics, Siberian Branch of Russian Academy of Science, Novosibirsk 630090, Russia

1. Introduction

Shock-wave/turbulent boundary layer interactions (SWTBLI) are prevalent phenomena in high-speed flights, which could cause large flow separation and high wall heat flux and strong pressure fluctuation, therefore, affect significantly the aero-thermodynamic loads of the vehicles and the performance of propulsion systems. Among all kinds of SWTBLI, the supersonic expansion–compression corner is an important flow configuration consisting in the forebody, intake, combustion chamber and nozzle of high-speed flying vehicle[1]. In an expansion–compression corner, the supersonic flow is accelerated and turned through an expansion fan formed at the expansion corner (EC), then compressed by a shock-wave formed around the compression corner (CC)[1]. The boundary layer in the compression corner region can be either attached or separated, depending on the strength of the shock-wave. This kind of flows is complicated and essentially non-equilibrium due to the strong interaction among the turbulence, expansion-wave, and shock-wave.

In despite of the important significance of the expansion–compression corner flow, it's less investigated and understood than the supersonic compression corner or the impinging shock-wave/boundary layer interaction[2]. The early researches mainly focused on the expansion and curvature effects of the expansion side of the configuration, including the increase of the boundary layer thickness[3,4], the reduction of turbulence and its transport capability[5-8], the stabilization and the relaminarization of the boundary layer[9-13] during the expansion process. Zheltovodov et al.[14-17] conducted systematically measurements on the expansion–compression corner in early 1990s and concluded three basic characteristics of the flow regimes: (1) the attached flow for small β, (2) the appearance of a local separation zone in CC with a free separation point at moderate β, (3) formation of large-scale separated flow with a fix separation point when β is large enough. The relation of the characteristic length of flow separation L_c with the incoming boundary layer thickness and Mach number was also concluded by Zheltovodov et al.[18]. The appearance of Görtler vortices were also reported with the help of the surface pattern visualization. Later, Zheltovodov et al.[18, 19], Horstman and Zheltovodov[20] and Borisov et al.[21] conducted combined researches of numerical simulations and experimental measurements and found that Reynolds-Averaged Navier–Stokes (RANS) method with different turbulence models could not accurately predict the flow field, including the separation and reattachment positions, and distributions of surface skin friction and heat transfer coefficients. Therefore, the application of RANS-based approach for in-depth researches of high-speed aerodynamics is quite limited, due to the incapability of turbulence model in predicting complex non-equilibrium flows. More accurate and fidelity methods such as direct numerical simulation (DNS) and large-eddy simulation (LES) would be necessary.

In DNS and/or LES, small-scale turbulent fluctuations can be either directly resolved or modelled up to sub-grid scale (SGS) level. Therefore, they can provide detailed flow information and accurate predictions. Nowadays, DNS and LES are playing very important roles in turbulence simulation and modelling.[22] The first LES of the expansion–compression corner flow was conducted by Knight et al.[23] They adopted Monotone Integrated Large Eddy Simulation (MILES) with the second-order Godunov scheme for spatial discretization on unstructured tetrahedral mesh.

Their LES has shown general good agreement with the experimental measurements. Recently El-Askary[24] conducted a LES with the same flow condition as Knight et al.[23] The MILES methodology was again adopted together with the second-order upwind-biased scheme. The better predictions than those of Knight et al.[23] were reported, which could be attributed to the improved mesh quality.

In this paper, we will present DNS of the expansion–compression corner flow at Mach 2.9 and a 25° deflection angle. The Reynolds number considered are Re_δ=20000, Re_δ=40000 and Re_δ=80000, corresponding to the flow conditions of previous LES study[23,24] and the experimental measurements of Zheltovodov et al.[25], respectively. The DNS results are validated by comparing with published experimental measurements and other DNS/LES data. The detailed turbulence structures and flow statistics in the backward-facing step interaction region are analysed and the Reynolds number effect is also discussed.

2. Numerical Method

Three-dimensional unsteady compressible Navier-Stokes (N-S) equations in a general, time-invariant, curvilinear coordinate system are numerically solved for the present research.

The Euler terms of the NS equations are solved by using the newly developed seventh-order low-dissipation monotonicity-preserving (MP7-LD) scheme[26]. After all the spatial terms are solved, the residual terms are integrated in time by using the explicit three-step third-order TVD Runge-Kutta scheme.

In DNS/LES of turbulent boundary layer, the inlet turbulent fluctuations need to be artificially constructed. Lots of efforts have been made in developing inflow turbulence generation technology. In the present research, the digital filter method proposed by Touber and Sandham[27] is used to generate synthetic inflow turbulence. This method is very competitive with the widely used rescale-reintroduce method[28,29] in terms of the domain requirement of the transition region[30] and thus has the benefit of avoiding any artificial periodicity.

After the inflow fluctuations are generated, the supersonic inflow condition is used to prescribe the flow variables at the inlet plane, except for the subsonic portion of the boundary layer, where the pressure is extrapolated from the inner points. At the far field and the outlet plane, all the variables are extrapolated using known values inside the computational domain, which is efficient and stable[31]. At the bottom wall, the isothermal nonslip condition with the adiabatic temperature of $T_W = 2.51T_0$ at the wall is used. The periodic condition is used in the spanwise direction.

The computational domain is sketched in Fig. 1, scaled with the reference length of the nominal boundary layer thickness δ_{ref} at the reference plane at x=0 and the expansion corner location (EC) is placed $4\delta_{ref}$ downstream the reference plane. To be consistent with the experiment of Zheltovodov et al.[17] as well as the LES of Knight et al.[23] and El-Askary[24], the deflection angle of the backward-facing step is set to be $\beta = 25°$, and the vertical distance between the two plate is $h = 3\delta_{ref}$. The detailed information about the size of the domains and meshes of the three cases are given in Table 1. Unless otherwise noted, all the lengths in the rest of the paper are scale with δ_{ref}. Case 1 has finer mesh resolution than the Case 2 and Case 3, and they both satisfy the DNS spatial resolution recommended by Sagaut[32] for wall-bounded turbulent flows.

Table 1 Domain size and mesh parameters

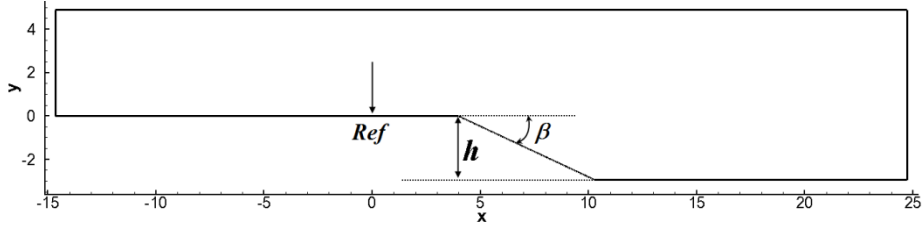|	Re	x_0	x_{max}	y_{max}	z_{max}	$N_x \times N_y \times N_z$	$(\Delta x^+_{ref}, \Delta x^+_{min})$	Δy^+_1	Δz^+
Case 1	20000	-16.9	30	6	6	1420×120×256	(5.1, 1.1)	0.55	4.3
Case 2	40000	-13.6	30	6	5	2020×120×300	(7.1, 1.4)	0.45	5.7
Case 3	80000	-11.9	23	6	3	2020×120×400	(7.4, 1.5)	0.68	4.3

Fig. 1. Sketch of the computation domain.

The present DNS mesh is straight and perpendicular in all three directions, except for in the ramp region, where the mesh lines are gradually turned towards the ramp surface in order to preserve both the orthogonality and smoothness of the mesh. The mesh is concentrated near the reattachment point to achieve the local grid resolution of $\Delta_x^+ \approx 1$ for the capture of the small-scale turbulent structures there. The resolution at the reference plane is listed in Table 1.

The inflow Mach number is 2.9. The flow is expected to be fully developed at the reference plane x=0, at which the boundary layer parameters are listed in Table 2.

Table 2 Boundary layer parameters at the reference plane

	Cf	δ	δ^*	θ	Re_δ	Re_{δ^*}	Re_θ
Case 1	0.00224	1.0	0.45	0.077	19983.8	8950.8	1531.8
Case 2	0.00186	1.0	0.42	0.076	40934.2	17203.8	3090.4
Case 3	0.00138	1.0	0.43	0.076	80051.0	34567.2	6140.7

3. Results and Discussions

To validate the present DNS results, we firstly compared the velocity profile at x=2, where the boundary layer is still in the state of equilibrium, with the high-Re experimental measurement of Zheltovodov et al. [16] in Fig. 2 (a). The good agreement between the present three cases and the measurement can be confirmed. The van Driest transformed velocity in wall unit u_{vd}^+ is plotted in Fig. 2 (b), together with the law of wall and the measurements in the incompressible boundary layers of Murlis et al.[33] and Erm and Joubert[34]. It can be seen from Fig. 2 (b) that, the velocity profile in the linear layer and log layer perfectly matches the incompressible law of wall with the standard von Kármán constant. With the increase of the Reynolds number, the log layer extends and the wake layer becomes higher. Overall the agreement between the present DNS and the incompressible measurements is satisfactory in the log layer, and the discrepancy in the wake layer can be attributed to the Reynolds number effects.
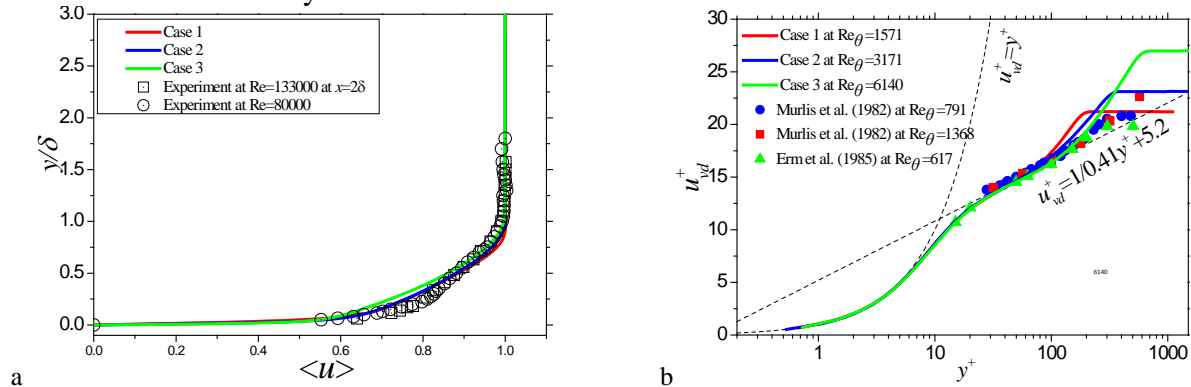
Fig. 2. Mean velocity profile at x=2. (a) is in boundary unit and (b) is in wall unit.

The comparison of the mean wall pressure distributions from three present DNS as well as previous LES results[23, 24] and experimental data of Zheltovodov et al.[25] are shown in Fig. 3 (a). It can be seen that, the pressure is reduced sharply at EC position then gradually till the middle of the ramp, i.e. at the foot of the front shock-wave, where the wall pressure begins to rise. A pressure-plateau can be identified in the region of $8 < x < 11$ corresponding to the location of the separation

bubble. After interaction with the rear shock-wave, the pressure is largely increased. With the increase of Reynolds number, the level of the pressure-plateau is slightly reduced and the pressure after the rear shock is increased more rapidly, which agrees with the trend of the experimental data. Overall, the wall pressure profiles of the present cases match well with the experiments and the LES data.

From the wall pressure gradient $\frac{dP_W}{dx}$ in Fig. 3 (b), we can see the two positive peaks, which correspond to the two legs of the λ-shock respectively. With the increase of the Reynolds number, the first peak moves downstream and the second peak moves upstream, which mean the decrease of the angle between the two legs of the λ-shock. Therefore, it can be deduced that, the two peaks will move close to each other with further increase of Reynolds number and finally merge together when the Reynolds number gets to the infinity. The value of the second peak also increases with the increase of the Reynolds number, due to the reduction of the viscous effect.
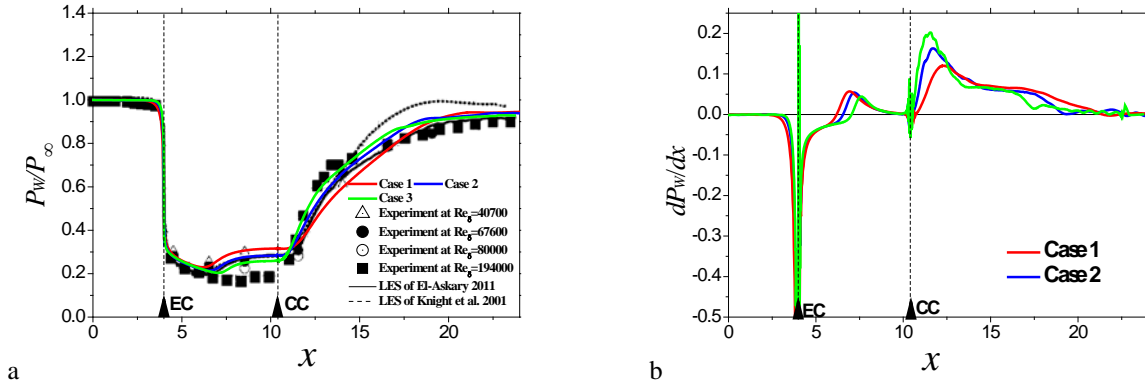

Fig. 3. Mean wall pressure (a) and wall pressure gradient distribution (b). The pressure gradient is normalized with P_∞/δ_{ref}. P_∞ is the static pressure of the incoming flow.

The instantaneous numerical density schlieren applying $0.8e^{-10(|\nabla\rho|-|\nabla\rho|_{min})/(|\nabla\rho|-|\nabla\rho|_{max})}$ of three flow cases are shown in Fig. 4. The experimental schlieren of Zheltovodov et al.[14] at $Re_\delta=$ 190000 is also given for quantitatively comparison. The λ-shock system can be seen clearly from the schlieren of the DNS. All the three pictures in Fig. 4 have similar flow patterns, and we can observe the weakening of the turbulent structures with the increase of their sizes during the expansion process. From the DNS results, we can see the flow in the separation bubble is less fluctuant, which mean the flow in it could be laminar.
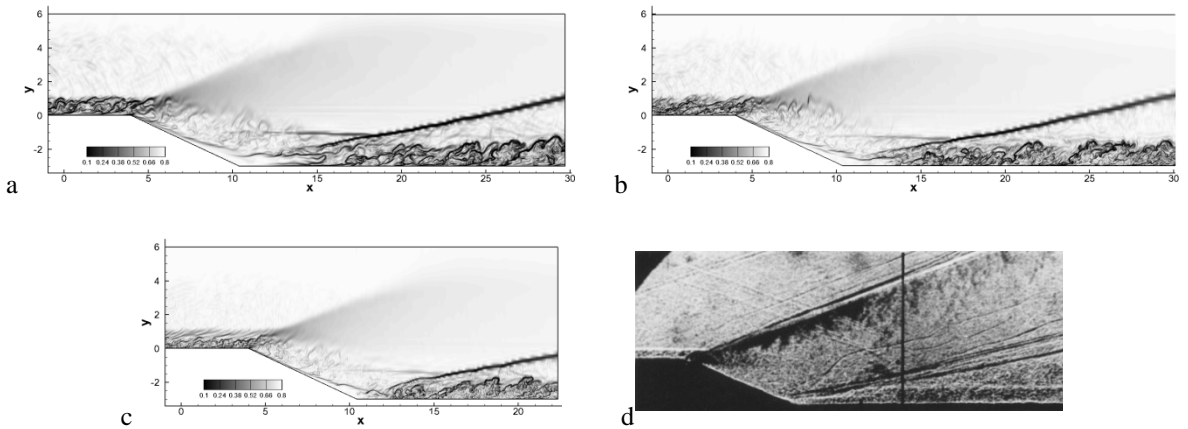

Fig. 4. The instantaneous density schlieren of Case 1 (a), Case 2 (b) Case3 (c) and the experiment observation of Zheltovodov et al. [14] at $Re_\delta = 190000$ (d)

The mean skin friction Cf are plotted in Fig. 5, in which we can see that The skin friction has a strong spike at EC, which is caused by the sudden change of the surface geometry. After the spike, the skin friction gradually decreases and at about the half of the ramp, the skin friction has a plateau region with negative values, which indicates the existence of the separation region with reverse flows. The plateau value of present DNS cases and other published data collapses, which means it is independent of flow Reynolds number. The separation point is located just downstream the first positive peak of the wall pressure gradient (see Fig. 3 b), which is also the position of the foot of the front shock. Downstream the compression corner, with the increase of the adverse pressure gradient, the skin friction decreases again and reaches the minimum value. After that, Cf begins to increase and the reattachment point can be identified according to $Cf = 0$. Further downstream, the increase of Cf slows down, which indicates the recovery of the turbulent boundary layer towards another equilibrium status.
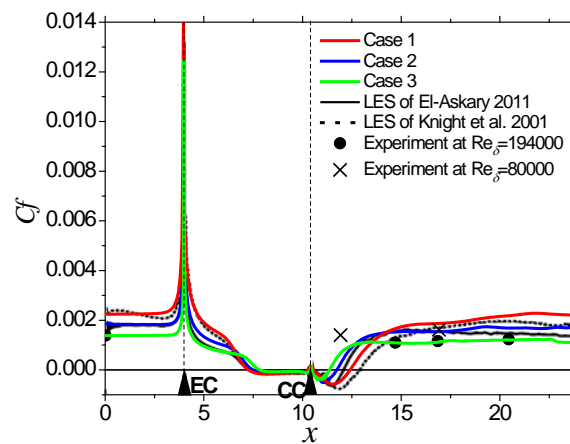

Fig. 5. Mean skin friction distribution.

According the skin friction, the reduction of the size of the separation region and the forward movement of the reattachment with the increase of the Reynolds number can be confirmed and with the increase of the Reynolds number, the recovery of the skin friction downstream the reattachment is also faster. In general, the predicted skin frictions of the present DNS are in good agreement with the experimental data of Zheltovodov et al.[14] as well as two previous LES results. Comparing all the simulation results, it can be seen that, the discrepancy of all the simulations are mainly presented in region downstream the compression corner location, where the flow is dominated by the SWTBLI. The difference in separation bubble size and reattachment point could be primarily due to Reynolds number effect that leads to the generation of small turbulent structures by the SWTBLI. As there is limited experimental data available in this region, it is not possible to judge which simulation produces better prediction of the skin friction than others.

In Figs. 6 *a–c*, predicted the mean surface streamlines in the 3D region of the three cases are compared. Downstream the separation line, several periodic longitudinal convergence and divergence lines located along the plate width can be identified. Such the periodic lines have been observed also in experiments[14], however, they have been not very distinct at β = 25° as compared with similar ones observed at the higher deflection angle $\beta = 45°$ (see Fig. 6 *c*).

This flow topology is also observed in two-dimensional compression corner flow experiments by using surface visualization technology[35] and numerical simulations by using LES[36], which is considered as the evidence of Görtler type vortices. The topologies of the surface streamlines of the predicted three cases are identical and the spanwise distances between the convergence lines are all at the scale of δ_{ref}, which are independent of the Reynolds number and smaller than the value in the compression corner flow LES of Loginov et al.[36], who reported a spanwise scale about 2δ. However, in accordance with experiments by Zheltovodov et al.[14] the spanwise scale is also about

$2\delta_R$ downstream the backward-facing step if the reattaching boundary-layer thickness δ_R to be used as a reference value.
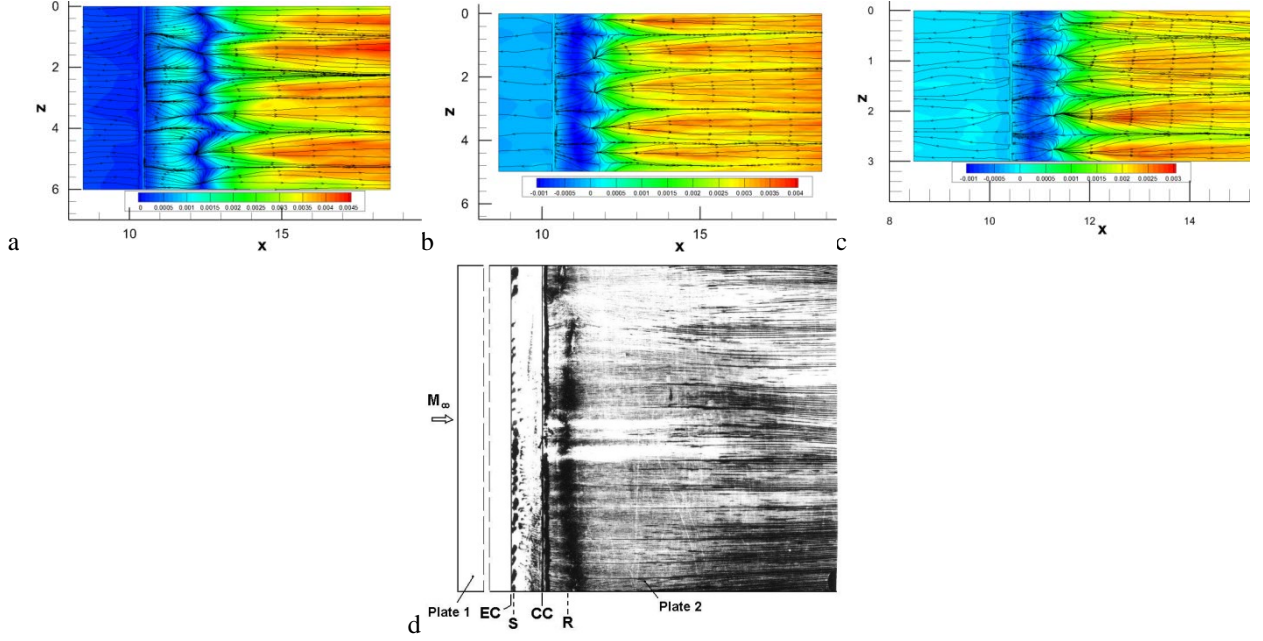

Fig. 6. Time averaged skin friction coefficient and surface streamlines around the reattachment line for (a) Case 1, (b) Case 2, (c) Case 3, (d) Experimental surface flow pattern (oil flow visualization) at $\beta = 45°$, $Re_\delta = 194000$. (EC – expansion corner, CC – compression corner, S – separation line, R – reattachment line).

The normal Reynolds stress components and the turbulent kinetic energy (defined as $= 0.5\langle u_j'' u_j'' \rangle$) contours are shown in Fig. 7. During the expansion process, all components of normal Reynolds stresses are suppressed. Downstream CC, they are all greatly amplified due to the interaction with the shock-wave. The maximum turbulent kinetic energy can be found near the reattachment point and its peak is placed in the middle of the boundary layer rather than in the near wall region, which means the fluctuations are dominated by the turbulent structures detached from the wall. Further downstream, the normal Reynolds stresses in the outer region of the boundary layer are dissipated and $\langle u'' u'' \rangle$ and $\langle w'' w'' \rangle$ begin to increase in the near wall region, which indicates the regeneration of wall turbulence during the recovery of the boundary layer.
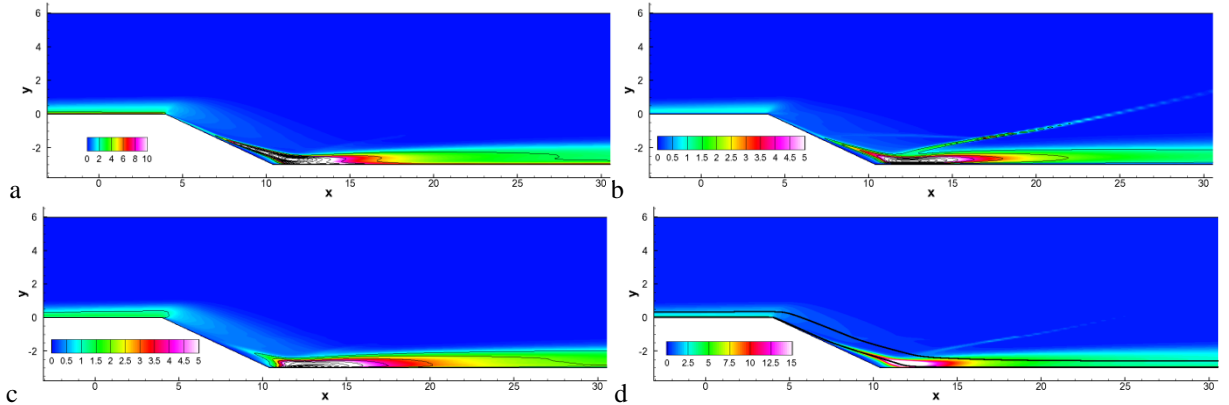

Fig. 7. Components of Reynolds normal stresses. (a): $\langle u'' u'' \rangle$, (b): $\langle v'' v'' \rangle$, (c): $\langle w'' w'' \rangle$, (d): Turbulent kinetic energy. All variables are normalized with the square of friction velocity u_τ at the reference place. Two streamlines are shown in (d) with black solid lines.

It is worth to note that, the evolution of the turbulence stress in the ramp region is different in inner layer and outer layer regions. In the outer layer, the turbulent fluctuations keep decreasing in

the whole ramp region. However, for the inner layer, the Reynolds stresses are reduced sharply near EC, and then begin to increase almost immediately after EC. Therefore, the differences between the inner and the outer layers become more and more distinguishable during the evolution along the ramp. To investigate this property, two streamline traces are introduced, one from the near-wall region (S1: x=0, y=0.03) and the other from the middle of the boundary layer (S2: x=0, y=0.35) at the reference plane, as shown in Fig. 7 (d). The normal Reynolds stresses evolution along these two streamlines are plotted in Fig. 8. It can be seen that along the streamline S1, $\langle u''u'' \rangle$ and $\langle w''w'' \rangle$ have shown significant reduction within a shorter distance after EC, whilst $\langle v''v'' \rangle$ has only negligible oscillation around EC position. Downstream EC, all compounds of the Reynolds stresses increase along the ramp surface. The rate of the increase is largely amplified after the interaction with the front shock at $x \approx 7$, and it continues after the interaction with the rear shock at CC. The peak of the normal Reynolds stresses can be found near the reattachment point.

In contrary, along the streamline S2, all normal Reynolds stress components are gradually reduced downstream EC, until the region where turbulence is amplified by the strong SWTBL, and then the increase of all compounds of normal Reynolds stresses can be seen. Therefore, it is clear that the turbulence in the inner layer and the outer layer has undergone completely different evolution process, which means the different turbulence suppression and re-development mechanisms in the inner and outer layers along the ramp surface.
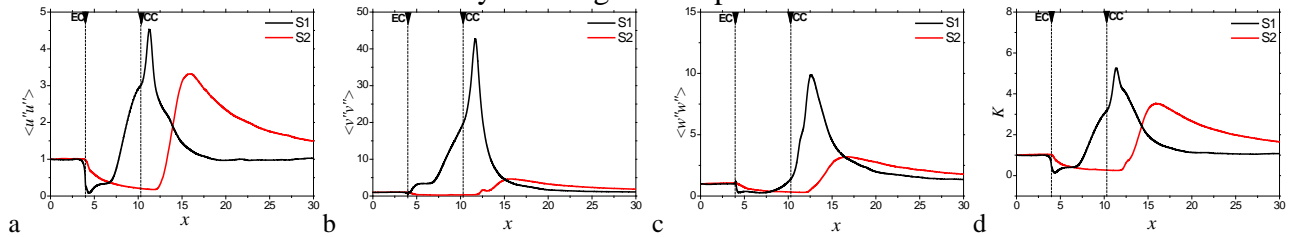

Fig. 8. Evolution of $\langle u''u'' \rangle$ (a), $\langle v''v'' \rangle$ (b), $\langle w''w'' \rangle$ (c), and K (d), along the streamlines S1 and S2. All variables are normalized with their values at the reference plane.

The instantaneous turbulent flow field will be analyzed to investigate the turbulence structures. Firstly, the streamwise velocity fluctuation u_s'' along two planes containing streamlines S1 and S2 respectively are shown in Fig. 9. For the streamline (S1) plane, which is in the near-wall region, we can see the classic streamwise elongated streaks in the upstream undisturbed boundary layer region and the distance between two neighbouring low-speed streaks is about $\Delta z^+ = 100$, in agreement with other DNS studies[37],[38]. Dowstream EC, the strength of velocity fluctuations is weakened. However, the streaky structures are still preserved and their scale is largely increased. From the second half of the ramp, we can see large-scale streaks with a spanwise length scale of about δ_{ref} and a streamwise length scale of about $5\delta_{ref}$. Downstream the reattachment point, the large-scale streaks become unstable and break down to generate more small-scale structures. After $x = 15$, the classic streaky structures as seen in the upstream undisturbed boundary layer are formed, which promote the near-wall turbulence recovery towards the equilibrium status.

In contrary, the streamwise velocity fluctuation along the streamline (S2) plane presents weak and less organized structures in the upstream undisturbed boundary layer and these fluctuations are consistently suppressed over the ramp region until the flow reattachment point. After $x = 15$ in the mixing layer region, we can see some large-scale structures in the boundary layer recovery region, which is contributed by the large-scale turbulent coherent structures in the mixing layer.
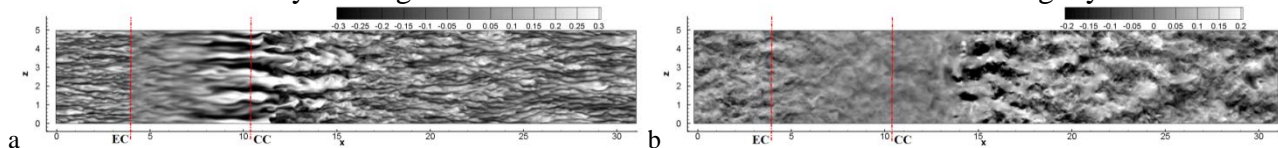
Fig. 9 Streamwise velocity fluctuation along the streamlines S1 (a) and S2 (b).

The turbulent coherent structures are further visualized with the λ_{ci} criterion, which was proposed by Zhou et al.[39] as the representation of the swirling strength. The iso-surface of λ_{ci} colored with the instantaneous x-vorticity ω_x is shown in Fig. 10. The coherent structures in the undisturbed boundary layer present classic streamwise elongated hairpin vortices.

In the ramp region, we can barely see any structures, which indicate the expansion process greatly reduce the swirling strength of the turbulence. Near the reattachment line in Fig. 10 (c), we can see some large-scale coherent structures in the near-wall region, indicating the Görtler vortices. In the recovery region, we can see lots of detached structures in the middle of the boundary layer, which is generated by the free shear in the mixing layer. These structures are dissipated with the recovery of the boundary layer, while attached hairpin structures are gradually regenerated.
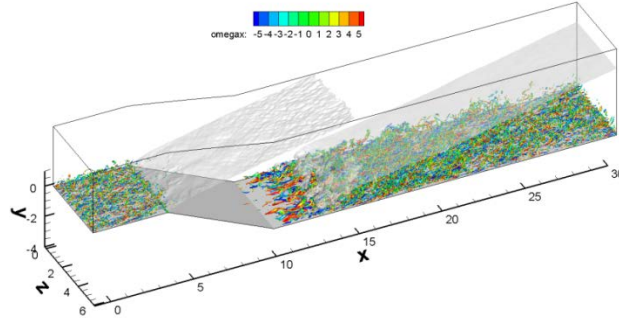

Fig. 10. Turbulence coherent structures visualized with the iso-surface of $\boldsymbol{\lambda_{ci}}$ equaling to 0.8% of its global maximum and coloured with the x-vorticity. The expansion-wave and shock-wave are visualized by using the iso-surface of
$$p = 0.6p_0.$$

The visualization of turbulent coherent structures in the ramp region is enhanced by using the iso-surface of $\lambda_{ci} = 0.16\%\lambda_{ci,max}$ in Fig. 11, in which the evolution of the two-layer structures of turbulence along the ramp can be seen. The turbulent coherent structures from the outer part of the undisturbed boundary layer are gradually damped with the loss of their coherence during the expansion process. In the inner layer, however, the quasi-streamwise structures are preserved all the way along the ramp. Therefore, the separation line, the large-scale quasi-streamwise vortices can be seen very clearly. These structures have larger scale in both spanwise and streamwise than the streamwise vortices in the undisturbed boundary layer and contribute to the streamwise elongated streaks in the near-wall region of the ramp, as shown in Fig. 9 (a). Further downstream, the size of these quasi-streamwise structures becomes larger, and near CC, the spanwise size between these structures is about δ_{ref}, which is the same size with the Görtler vortices.
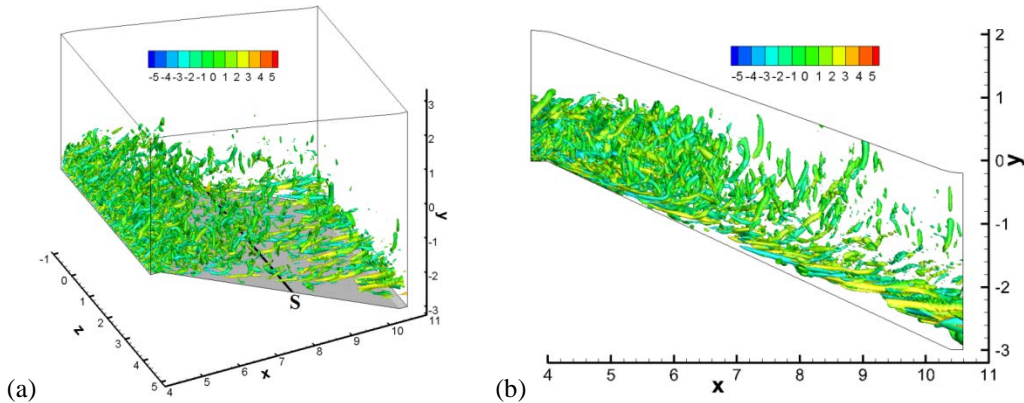

(a)　　　　　　　　　　　　　　　(b)

Fig. 11. Turbulent coherent structures in the ramp region. $\lambda_{ci} = 0.16\%\lambda_{ci,max}$ is used to visualize coherent structures. (b) is the view from the z direction.

4. Conclusions

The Mach=2.9 supersonic turbulent flow in an expansion-compression corner with 25° decline angle at Re_δ=20000, Re_δ=40000 and Re_δ=80000 are studied by using DNS with the high-order low-dissipative numerical scheme. The DNS results are well validated by comparing the wall properties in both equilibrium boundary layer and interaction regions with published experimental measurements and other DNS/LES data. The detailed turbulence structures and flow statistics in the backward-facing step interaction region are firstly reported and analysed.

It was found that with the increase of Reynolds number, the reattachment line moves upstream and the size of the separation bubble decreases. Despite the skin friction increases after the flow reattachment are steeper at higher Reynolds number case, the lower Reynolds number case reaches higher skin friction in the recovery region.

In the ramp region, the turbulence motions and structures are at first largely suppression after the expansion-waves emitted from expansion corner, and then amplified due to the interaction with the shock-wave formed at compression corner region. During the expansion process, a two-layer turbulence structure is observed, in which the turbulence in the outer layer is suppressed over entire ramp. In the inner layer, however, the turbulence is merely suppressed in a small region around the corners and then enhanced in the rest of the ramp. Therefore, a thin layer with high level of turbulent fluctuations can be observed in the region close to the ramp surface. It is also found that although the turbulence motion is suppressed in certain ramp region, the quasi-streamwise coherent structure is still preserved. After the flow reattachment, the large-scale Görtler vortices induce strong velocity fluctuations in the near-wall region, which leads to 'quick' regeneration of wall turbulence and recovery of the boundary layer to equilibrium status.

The large-scale Görtler vortices are correlated with the rapid increase of skin friction near the reattachment line. From the analysis of wall streamline, we can see a typical saddle-node combination with a characteristic size of δ_{ref}.

Acknowledgement

REFERENCES

1. **Knight D., Yan H., Panaras A.G., and Zheltovodov A.A.** Advances in CFD prediction of shock wave turbulent boundary layer interactions. // *Progress in Aerospace Sciences*. 2003. Vol. 39. P. 121-184.
2. **Knight D.D., and Zheltovodov A.A.** Ideal-Gas Shock Wave–Turbulent Boundary-Layer Interactions (STBLIs) in Supersonic Flows and Their Modeling: Two-Dimensional Interactions. *Shock Wave-Boundary-Layer Interactions.* Eds. H. Babinsky, J. Harvey. Cambridge University Press, London, 2011. P. 137-201.
3. **Dawson J., Samimy M., and Arnette S.** Effects of expansions on supersonic boundary layer: Surface pressure measurements // *AIAA J.* 1994. Vol. 32, №. 11. P. 2169-2177.
4. **Arnette S., Samimy M., and Elliott G.** The effects of expansion on the turbulence structure of a compressible boundary layer // *J. of Fluid Mech.* 1998. Vol. 367, P. 67-105.
5. **Morkovin M.** Effects of high acceleration on a turbulent supersonic shear layer // Proc. the Heat Transfer and Fluid Mechanics Institute, Stanford University, 1955.

6. **Thomann H.** Effect of streamwise wall curvature on heat transfer in a turbulent boundary layer // *J. of Fluid Mech.* 1968. Vol. 33. P. 383-392.

7. **Lewis J., Gran, R., and Kubota T.** An experiment on the adiabatic compressible turbulent boundary layer in adverse and favorable pressure gradients // *J. of Fluid Mech.* 1972. Vol. 51, №. 4. P. 657-672.

8. **Adamson T.** Effect of transport properties on supersonic expansion around a corner // *Physics of Fluids.* 1967. Vol. 10, №. 5. P. 953–962.

9. **Narasimha R., and Sreenivasan K.** Relaminarization in highly accelerated turbulent boundary layers // *J. Fluid Mech.* 1973. Vol. 61. P 417-447.

10. **Dussauge J., and Gaviglio J.** The rapid expansion of a supersonic turbulent flow: role of bulk dilatation // *J. Fluid Mech.* 1987. Vol. 174. P. 81-112.

11. **Smith D., and Smits A.** The rapid expansion of a turbulent boundary layer in a supersonic flow // *Theor. and Computl Fluid Dyn.* 1991. №. 2. 3. P. 319–328.

12. **Page R., and Sernas V.** Apparent reverse transition in an expansion fan // *AIAA J.* 1970. vol. 8. P. 189–190.

13. **Zakkay V., Toba K., and Kuo T.** Laminar transitional and turbulent heat transfer after a sharp convex corner // *AIAA J.* 1964. Vol. 2. P. 1389–1395

14. **Zheltovodov A., Mecler L., and Schülein E.** Peculiarities of development of separated flows in compression corners after the expansion fans. Preprint № 10-87. Institute of Theoretical and Applied Mechanics, USSR Academy of Sciences, Novosibirsk, 1987 (in Russian).

15. **Zheltovodov A., and Schülein E.** Peculiarities of turbulent separation development in disturbed boundary layers // *Modelirovaniye v Mekchanike (Modelling in Mechanics).* 1988. Vol. 2. No. 1. P. 53-58 (in Russian).

16. **Zheltovodov A., Zaulichiy E. and Trofimov V.** Development of the models for calculations of the heat transfer in conditions of supersonic turbulent separated flows // *J. of Applied Mech. and Techl Phys.* 1990. Vol. 4. P. 90-104 (in Russian).

17. **Zheltovodov A., Zaulichiy E. and Trofimov V.** Gas dynamics and heat transfer in separated flows // *Russian J. of Theor. and Appl. Mech.* 1992. №. 2. P. 79-84.

18. **Zheltovodov A., Schülein E. and Horstman C.** Development of separation in the region where a shock interacts with a turbulent boundary layer perturbed by rarefaction waves // *J. of Applied Mech. and Tech. Phys.* 1993. Vol. 34. №. 3. P. 346-354.

19. **Zheltovodov A., Borisov A., Knight D., Horstman C., and Settles G..** The possibilities of numerical simulation of shock waves/boundary layer interaction in supersonic and hypersonic flows // *International Conference on the Methods of Aerophysical Research.* Novosibirsk, 1992. Part 2. P. 164-170.

20. **Horstman C., and Zheltovodov A.** Numerical simulation of shock waves/expansion fans—turbulent boundary layer interaction // *International Conference on the Methods of Aerophysical Research.* Novosibirsk, 1994. Part 2. P. 118-125.

21. **Borisov A., Zheltovodov A., Maksimov A., Fedorova N., and Shpak S.** Verification of turbulence models and computational methods of supersonic separated flows // *International Conference on the Methods of Aerophysical Research.* Novosibirsk, 1996. Part 1. P. 54-61.

22. **Moin P., and Mahesh K.** Direct numerical simulation: A tool in turbulence research // *Annual Review of Fluid Mech.* 1998. Vol. 30. P. 539-578.

23. **Knight D., Yan H., and Zheltovodov A.** Large eddy simulation of supersonic turbulent flow in expansion-compression corner // *Third AFOSR International Conference on DNS and LES.* 2001, Greydon Press, Columbus, OH, 2001. P. 183-194.

24. **El-Askary W.** Simulation of supersonic turbulent flow in the vicinity of an inclined backward-facing step // *Intern. J. of Comput. Fluid Dyn.* 2011. Vol. 25. №. 7. P. 407-423.

25. **Zheltovodov A., Trofimov V., Filippova E.** Influence of turbulence change on the heat exchange under the conditions of supersonic separated flows // IUTAM Symposium on Separated Flows and Jets. Abstracts. Novosibirsk, 1990. P. 273–274.

26. **Fang J., Li Z, Lu L.** An optimized low-dissipation monotonicity-preserving scheme for numerical simulations of high-speed turbulent flows // *J. Sci. Comput.* 2013. Vol. 56. P.67-95.

27. **Touber E., Sandham N.D.** Large-eddy simulation of low-frequency unsteadiness in a turbulent shock-induced separation bubble // *Theor. and Comput. Fluid Dyn.* 2009. Vol. 23. P.79-107.

28. **Lund TS, Wu X, Squires KD.** Generation of turbulent inflow data for spatially-developing boundary layer simulations // *J. Comput. Phys.* 1998. Vol. 140. P.233-258.

29. **Sagaut P., Garnier E, Tromeur E, Larcheveque L, Labourasse E.** Turbulent inflow conditions for large-eddy simulation of compressible wall-bounded flows // *AIAA J.* 2004. Vol. 32. P.469-477.

30. **Morgan B., Larsson J., Kawai S., Lele S.K.** Improving low-frequency characteristics of recycling/rescaling inflow turbulence generation // *AIAA J.* 2011. Vol. 49. P.582-597.

31. **Wasistho B., Geurts B.J., Kuerten J.G.M.** Simulation techniques for spatially evolving instabilities in compressible flow over a flat plate // *Comput. Fluids.* 1997. Vol.26. P.713-739.

32. Sagaut P. Theoretical background P. Large-Eddy Simulation // *In:* Wagner C., Hüttl T, Sagaut P., Eds. Large-eddy simulation for acoustics. Cambridge University Press. 2007. P. 89-127.

33. Murlis J., Tsai H.M., Bradshaw P. The structure of turbulent boundary layers at low Reynolds numbers // *J. Fluid Mech.* 1982. Vol. 122. P. 12-56.

34. Erm L.P., Joubert P.N. Low Reynolds number turbulent boundary layers // *J. Fluid Mech.* 1991. Vol. 230. P.1-44.

35. Zheltovodov A.A., Schulein E., Yakovlev V.N. Development of turbulent boundary layer at the conditions of mixed interaction with shock waves and expansion fans // Preprint 28–83,ITAM USSR Academy of Sciences, Novosibirsk. 1983 (in Russian).

36. Loginov M.S, Adams N.A, Zheltovodov A.A. Large-eddy simulation of shock-wave/turbulent-boundary-layer interaction // *J. Fluid Mech.* 2006. Vol. 565. P.135-69.

37. Spalart P.R. Direct numerical simulation of a turbulent boundary layer up to Re_θ=1410. *J. Fluid Mech.*. 1988. Vol. 187. P.61-98.

38. Kim J., Moin P, Moser R. Turbulence statistics in fully developed channel flow at low Reynolds number // J. Fluid Mech. 1987. Vol. 177. P. 133-166.

39. Zhou J., Adrian R.J., Balachandar S., Kendall T.M. Mechanisms for generating coherent packets of hairpin vortices in channel flow // J. Fluid Mech. 1999. Vol. 387. P.353-396.